



Article

The Performance of Nickel and Nickel-Iron Catalysts Evaluated As Anodes in Anion Exchange Membrane Water Electrolysis

Emily Cossar ¹, Alejandro Oyarce Barnett ^{2,3,*}, Frode Seland ⁴  and Elena A. Baranova ^{1,*} 

¹ Department of Chemical and Biological Engineering, Centre for Catalysis Research and Innovation (CCRI), University of Ottawa, 161 Louis-Pasteur Ottawa, ON K1N 6N5, Canada; ecoss089@uottawa.ca

² SINTEF Industry, Sustainable Energy Technology Department, New Energy Solutions Group, NO-7491 Trondheim, Norway

³ Department of Energy and Process Engineering, Norwegian University of Science and Technology, NO-7491 Trondheim, Norway

⁴ Department of Materials Science and Engineering, Norwegian University of Science and Technology, NO-7491 Trondheim, Norway; frode.seland@ntnu.no

* Correspondence: alejandrooyarce.barnett@sintef.no (A.O.B.); elena.baranova@uottawa.ca (E.A.B.); Tel.: +47-9300-3263 (A.O.B.); +(613)-562-5800 (ext. 6302) (E.A.B.)

Received: 29 August 2019; Accepted: 24 September 2019; Published: 27 September 2019



Abstract: Anion exchange membrane water electrolysis (AEMWE) is an efficient, cost-effective solution to renewable energy storage. The process includes oxygen and hydrogen evolution reactions (OER and HER); the OER is kinetically unfavourable. Studies have shown that nickel (Ni)- iron (Fe) catalysts enhance activity towards OER, and cerium oxide (CeO₂) supports have shown positive effects on catalytic performance. This study covers the preliminary evaluation of Ni, Ni₉₀Fe₁₀ (at%) and Ni₉₀Fe₁₀/CeO₂ (50 wt%) nanoparticles (NPs), synthesized by chemical reduction, as OER catalysts in AEMWE using commercial membranes. Transmission electron microscopy (TEM) images of the Ni-based NPs indicate NPs roughly 4–6 nm in size. Three-electrode cell measurements indicate that Ni₉₀Fe₁₀ is the most active non-noble metal catalyst in 1 and 0.1 M KOH. AEMWE measurements of the anodes show cells achieving overall cell voltages between 1.85 and 1.90 V at 2 A cm⁻² in 1 M KOH at 50 °C, which is comparable to the selected iridium-black reference catalyst. In 0.1 M KOH, the AEMWE cell containing Ni₉₀Fe₁₀ attained the lowest voltage of 1.99 V at 2 A cm⁻². Electrochemical impedance spectroscopy (EIS) of the AEMWE cells using Ni₉₀Fe₁₀/CeO₂ showed a higher ohmic resistance than all catalysts, indicating the need for support optimization.

Keywords: nickel; iron; ceria; OER; alkaline exchange membrane; electrolysis; anode

1. Introduction

As global warming and climate change concerns continue to rise, the concept of a “hydrogen economy” is becoming more and more important. This ideal is based on using hydrogen (H₂) as a clean, renewable fuel [1]. H₂ can also be used to store renewable energy through water electrolysis [2]. Water electrolysis utilizing anion exchange membranes (AEMs) is an emerging water electrolysis technology, used for its ability to produce hydrogen both efficiently and at low cost. Compared to traditional alkaline water electrolysis, which employ porous diaphragm separators, solid polymer electrolytes may provide certain advantages, such as lower gas crossover, improved efficiency, higher current densities, differential pressure operation and improved operation dynamics [3]. Unlike other solid polymer electrolyser technologies, such as proton exchange membrane water electrolysis (PEMWE), anion exchange membrane water electrolysis (AEMWE) technology has the potential to

operate without expensive noble-metal catalysts, such as iridium, ruthenium and platinum, in addition to low-cost materials for bipolar plates and current collectors. AEMWE, therefore, aims to combine the low costs of alkaline electrolysis with the high efficiency and flexibility of the proton exchange membrane (PEM) electrolysis design [3].

The theoretical thermodynamic potential for water electrolysis is 1.23 V at room temperature. To achieve a low activation overvoltage during electrolysis's operation, high performing oxygen and hydrogen evolving catalysts are required. As the goal of water electrolysis is its industrialization, catalyst cost is imperative. As such, the development of active non-noble metal catalysts is crucial to further develop and establish AEMWE technology. The number of studies addressing performance improvements through the development of new AEM materials, catalysts and membrane electrode assemblies (MEAs) have increased in recent years [4–13]. However, the water splitting performance reported for AEMWE is still lower than that of PEMWE [14,15], particularly when employing non-noble metal catalysts and lower concentrations of alkaline solutions, or water [16].

The water electrolysis process occurs through two simultaneously occurring half-cell reactions: the oxygen evolution reaction (OER) on the anode and the hydrogen evolution reaction (HER) on the cathode. OER kinetics are more sluggish than HER kinetics [17]; therefore, the performance of water electrolyzers heavily depends on the OER. Generally, the OER activity of non-noble electrocatalysts is high in alkaline environments [14]. Non-noble metal oxides are, therefore, of interest as catalysts for AEMWE. More specifically, catalysts based on Ni or Co (hydroxides, oxides, spinels and perovskites) and pyrochlores show good activity towards the OER in alkaline media. Ni-based electrocatalysts have been particularly well investigated, and include different ratios of Ni–iron (Fe), Ni–chromium (Cr) and Ni–molybdenum (Mo) oxide catalysts [6,18–23], amongst other bimetallics and alloys. Li et al. [18] studied various electrodeposited, Ni-bimetallic catalysts for OER. Among all tested metals, the NiFe catalyst showed the highest promotional effect, achieving the lowest overpotential of 256 mV at 0.5 A cm^{-2} with 10% iron incorporation. Similarly, Trotochaud et al. [20] tested multiple metal and mixed-metal oxide catalysts prepared by spin coating for OER. Their study showed that the $\text{Ni}_{90}\text{Fe}_{10}\text{O}_x$ catalyst obtained the lowest overpotential of 297 mV at 1 mA cm^{-2} .

The most widely accepted description of the Ni oxidation steps in alkaline media is through the Bode diagram, a simplified version of which is shown in Figure 1 below [24].

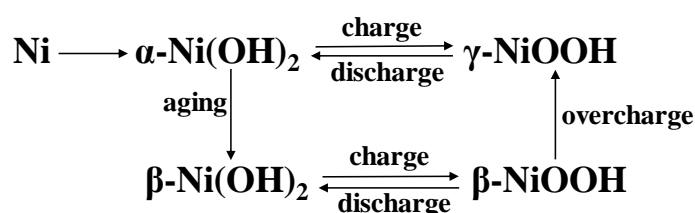


Figure 1. Nickel oxidation steps in alkaline media.

In an alkaline environment, nickel is first oxidized to the unstable $\alpha\text{-Ni(OH)}_2$ (about -0.5 V versus Hg/HgO). Prolonged exposure to an alkaline environment or slight anodic polarization brings it to the stable $\beta\text{-Ni(OH)}_2$ phase. Further polarization induces the oxidative deprotonation of $\beta\text{-Ni(OH)}_2$ to $\beta\text{-NiOOH}$ ($\sim 0.45 \text{ V}$ versus Hg/HgO or $\sim 1.38 \text{ V}$ versus RHE at pH 14), the active phase for OER [17]. Finally, further increasing the electrode potential will overcharge the nickel catalyst and bring it to the $\gamma\text{-NiOOH}$ phase, which is believed to be the highest-achievable Ni oxidation phase. It is most commonly assumed that the $\beta\text{-NiOOH}$ oxidation phase is most active towards the OER [17]. This oxidative deprotonation process to generate the catalytic species for the OER is not particular for nickel; it has been reported that cobalt, iron and manganese-based catalysts also deprotonate prior to oxygen evolution, in processes that are strongly pH-dependent [25–29].

Ceria (CeO_2) is an ionically conducting support that has been widely studied and applied in various electrochemical applications due to the advantageous metal support interactions (MSIs) that it may provide [30–32]. The MSIs occur through the unique properties of CeO_2 , such as oxygen storage

and release properties, and good ionic conductivity [33–35]. Using CeO₂ as a catalyst support can modify a catalyst's dispersion, minimize a catalyst's agglomeration and increase a catalyst's surface area. There are very few reports dealing with CeO₂ supports for non-noble metal catalysts for OER. Chen et al. [34] reported that the incorporation of CeO₂ into a copper oxide catalyst increased OER activity through strong electronic interactions between Ce⁴⁺ and Cu ions. They reported an optimal cerium content of 6.9%; further increasing the Ce content resulted in a less optimal Ce⁴⁺ distribution, and subsequently lower OER activity. Feng et al. [33] studied the incorporation of CeO₂ into FeOOH heterolayered nanotubes and concluded that the enhancement of OER's performance obtained through the incorporation of ceria into their catalyst was likely the result of the increased FeOOH/CeO₂ interfaces as well as the high oxygen storage capacity of the material. Haber et al. [36] developed a Ni_{0.3}Fe_{0.07}Co_{0.2}Ce_{0.43}O_x catalyst exhibiting good activity and stability towards OER. Said catalyst was further studied by Favaro et al. [35], who concluded that the incorporation of ceria into the catalyst does provide unique promotional catalytic properties towards OER. Finally, McCrory et al. [37], showed that their NiCeO_x material had the highest overpotential for OER compared to IrO_x and NiO_x, NiFeO_x, amongst other bimetallic electrocatalysts in 1 M NaOH. Preliminary cyclic voltammograms of the effect of ceria incorporation into the Ni catalyst are shown in Figure S1 of the Supplementary Information.

With respect to AEMWE studies, Seetharaman et al. [38] studied graphene oxide (GO) modified NiO electrode as an OER catalyst with enhanced electron conductivity and catalytic activity. A NiZnS ternary alloy was used at the cathode. The initial AEMWE performance of the electrodeposited catalysts on Ni foams was evaluated in the study. A Selemion™ AMV membrane (Asahi Glass Co. Ltd.) was used to prepare the membrane electrode assemblies (MEAs) and was sandwiched between the coated, foam electrodes. The AEMWE cell tests were performed using deionized water and concentrations of an alkaline solution (potassium hydroxide (KOH)) ranging from 0 to 5.36 M. They also tested various operating temperatures ranging from 30 to 80 °C. Increasing the concentration of the alkaline solution improved the initial cell performance, with current densities of approximately 65 and 140 mA cm⁻² observed for pure water and 5.36 M KOH, respectively, at 1.8 V and 30 °C. When using the 5.36 M electrolyte and holding the system at 1.8 V, the current density increased from 100 to 380 mA cm⁻² when increasing the operating temperature from 30 to 80 °C.

Xiao et al. [39] used electrocatalysts, such as Ni–Fe and Ni–Mo complexes, for the OER and HER in their MEAs. The Ni–Fe electrode was made using a solid-state electrochemical reduction procedure. Specifically, a solution containing Ni and Fe nitrates was sprayed onto a preheated Ni foam substrate and later electrochemically reduced by applying a cathodic current. The resulting loading of the catalysts was 40 mg cm⁻² for both electrodes, and the membrane and ionomer used were xQAPS. The performance achieved was 400 mg cm⁻² at 1.85 V in ultra-pure water. Ayers et al. [40] characterized AEMWE using non-noble metal complexes as catalysts for OER. They reported results for the ternary catalysts 30% Ni–Fe–Co/C and 30% Ni–Fe–Mo/C compared to 30% Ni–Fe/C and IrO₂. Although they reported very low current densities, between 5 and 40 mA cm⁻² at 1.8 V, the ternary catalysts showed higher performance compared to IrO₂ and 30% Ni–Fe/C.

Recently, Pavel et al. [41] developed and evaluated AEMWE using low cost transition metal catalysts. The commercial catalysts Acta 4030 (Ni/CeO₂-La₂O₃/C) and Acta 3030 (CuCoO_x) (Acta SpA, Italy) were used as HER and OER catalysts, respectively. The loadings of the HER and OER catalysts were 7.4 and 36 mg cm⁻², respectively. These catalysts were designed to withstand relatively mild alkaline conditions (pH 10–11). The authors explained the effect of HER loading on the kinetic contribution and performance of the AEM electrolysis. Results showed current densities between 60 and 300 mA cm⁻² at 1.8 V, as the HER catalyst's loading ranged from 0.6 to 7.4 mg cm⁻², while the OER catalyst's loading was kept constant at 36 mg cm⁻².

The aim of the presented work was to synthesize, characterize and electrochemically evaluate nanosized nickel-based electrocatalysts for the OER. Ni, Ni₉₀Fe₁₀ and Ni₉₀Fe₁₀/CeO₂ catalysts were synthesized by a scalable method, characterized by scanning and transmission electron microscopy (SEM and TEM), X-ray diffraction (XRD) and electrochemically evaluation using a conventional

three-electrode electrochemical cell. The Ni-based electrocatalysts were also evaluated as anodes in real AEMWEs and compared to commercially available noble metal-based anode electrodes. This paper includes a study on the influence of the alkaline electrolyte concentration on the catalytic activity of the OER; ex-situ, three-electrode OER measurements and in situ AEMWE performances are compared at 1 M and 0.1 M KOH concentrations.

2. Results and Discussion

2.1. Scanning and Transmission Electron Microscopy

Figure 2a,b shows TEM images of the as-synthesized Ni and Ni₉₀Fe₁₀ nanoparticles (NPs), respectively. Using the scale on the image, it was possible to approximate a particle size of around 4–6 nm, agglomerated into larger clusters of NPs.

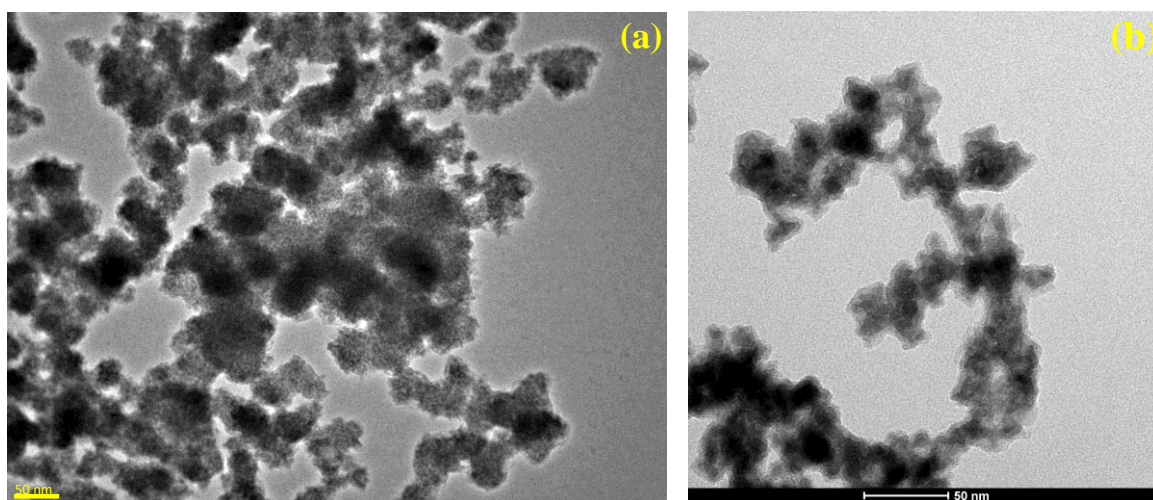


Figure 2. TEM of (a) Ni and (b) Ni₉₀Fe₁₀ nanoparticles (NPs).

Figure 3a–d represents SEM images of the anodes used in the AEMWE prior to experiments. Low magnification images are displayed to show how the bulk electrode surfaces differ from each other. Comparisons with the Ni, Ni₉₀Fe₁₀ and Ni₉₀Fe₁₀/CeO₂ electrodes are shown in Figure 3b–d, respectively. The Ir black benchmark shown in Figure 3a, shows a more porous electrode with a clearer presence of particles making up the electrode surface. Although the same ink preparation and electrode spraying procedure was used for all electrodes, the Ni-based electrode fabrication procedure may need further optimization. The Ni anode shows an almost flaky electrode surface, which was very similar to results obtained for the Ni₉₀Fe₁₀ electrode surface. The Ni₉₀Fe₁₀/CeO₂ electrode shows relatively flat surface with large cracks in it, which is likely the result of having to spray twice as much ink onto the membrane to get the same Ni loading, as 50 wt% of this catalyst is CeO₂ support. Furthermore, increasing the magnification of the Ni-based anodes did not present a more detailed electrode surface, hence why they were kept at a lower magnification than Ir.

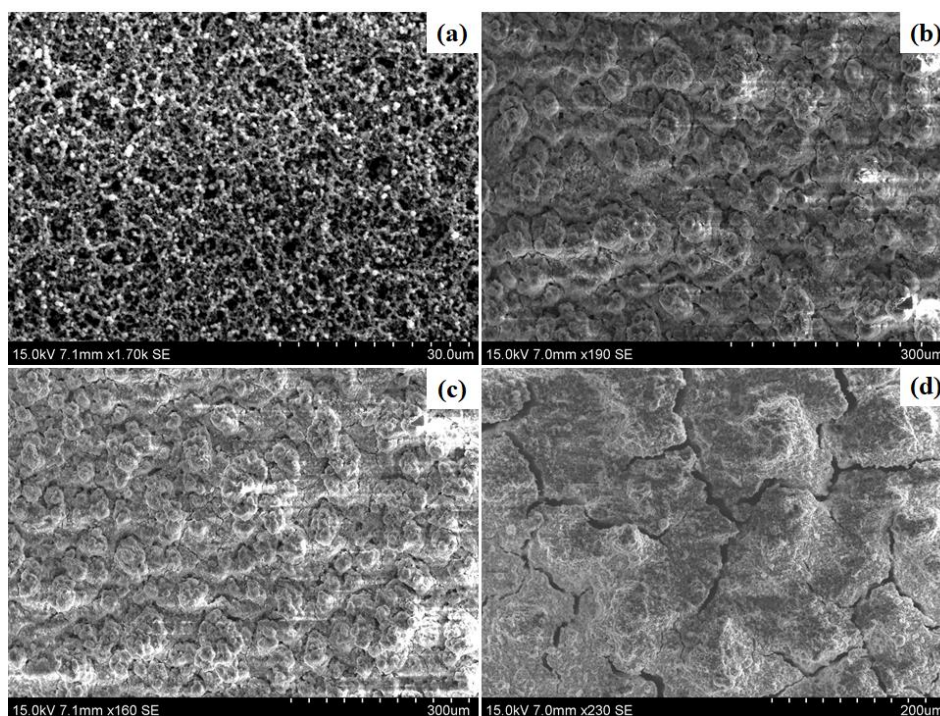







Figure 3. SEMs of (a) Ir black, (b) Ni, (c) Ni₉₀Fe₁₀ and (d) Ni₉₀Fe₁₀/CeO₂ anodes of the catalyst coated membranes. The magnifications of the images are 30, 300, 300 and 200 μm , respectively.

2.2. X-ray Diffraction

The XRD patterns of the Ni and Ni₉₀Fe₁₀ NPs are shown in Figure 4. XRD was not used to characterize the supported Ni catalyst, as ceria is also a face centered cubic (FCC) [32], and therefore, interferes with the main nickel diffraction peaks. As can be seen in Table 1, both samples include a mixture of Ni and β -Ni(OH)₂—the stable Ni(OH)₂ phase. In the Ni₉₀Fe₁₀ XRD pattern, the peak identified with the circle icon could be Ni (111) or Fe (110) [42,43]. Possible salt contamination can occur due to the synthesis method; however, catalyst samples were washed multiple times with water prior to XRD measurements to remove all NaCl. The possible presence of NaCl was ruled out due to the absence of particular sharp peaks in the XRD spectra [44]. Having both Ni and Fe in the same peak position, and the slight shift between the Ni(III) peaks shown in the Ni XRD, indicated the potential formation of an alloy material. Additionally, the broad peak shown in the Ni₉₀Fe₁₀ pattern reflects the very small particle size observed in the TEM image of the synthesized materials, shown in Figure 2.

Table 1. XRD results [42,43].

Icon on Figure 4	Experimental 2θ [deg]	Corresponding Compound; Reported 2θ [deg]
Diamond 	33.78	β -Ni(OH) ₂ (100); 33.1
Pentagon 	44.65	Ni (111); 44.45
Circle 	45.37	Ni (111); 44.45 Fe (110); 44.9
Triangle 	59.99	β -Ni(OH) ₂ (110); 59.1
Square 	70.68	β -Ni(OH) ₂ (103); ~71

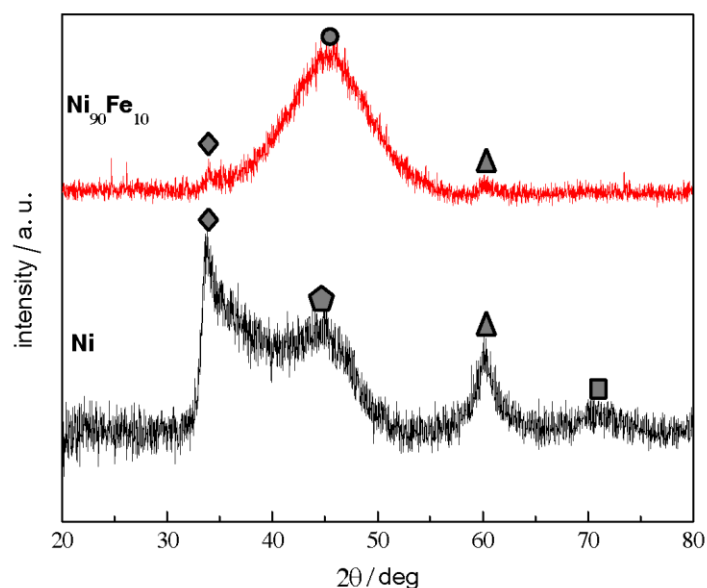


Figure 4. XRD results for Ni (black) and Ni₉₀Fe₁₀ (red) NPs.

2.3. Electron Energy-Loss Spectroscopy

Figure 5 summarized an EELS spectrum taken for the Ni₉₀Fe₁₀/CeO₂ material. In Figure 5a, it is possible to see, in orange, the region of the STEM image where the analysis was carried out. The region in yellow was used for drift correction. As shown in Figure 5b, within the orange region, two sections were analyzed; the first section shows a cloudier area, while the second section shows a clearer structured area. As seen in Figure 5c, the first region mostly consisted of the Ni and Fe metals in the sample, while the second region mostly consisted of the CeO₂ support. This observation is also seen in the EELS mapping found in Figure S5 of the Supplementary Information of this article. For TEM, STEM and EDX, characterization of the Ni₉₀Fe₁₀/CeO₂ catalyst, see Figures S2–S4 in the Supplementary Information.

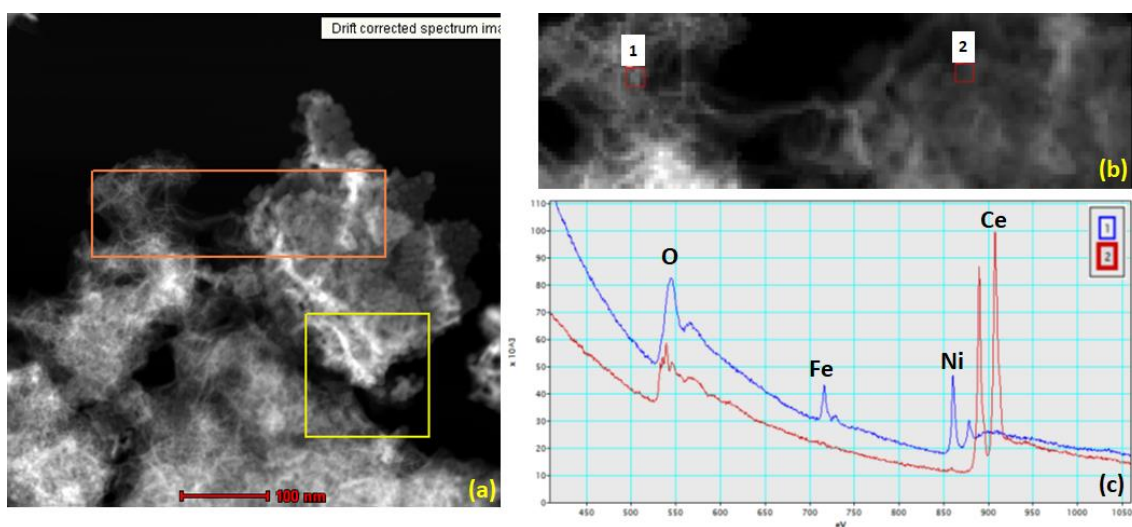


Figure 5. EELS results for Ni₉₀Fe₁₀/CeO₂. (a) The area of STEM image that was analyzed in orange, (b) shows the regions within the orange area that were analyzed and (c) shows the results of the analysis of the two regions.

2.4. OER Experiments

In the cyclic voltammograms (CVs) shown in Figure 6a, the overpotentials for OER in 1 M KOH can be summarize as $\eta_{\text{Ir black}} < \eta_{\text{Ni}_{90}\text{Fe}_{10}/\text{CeO}_2} < \eta_{\text{Ni}_{90}\text{Fe}_{10}} < \eta_{\text{Ni}}$, where the onset potential for OER of Ir occurs at ~ 0.524 V (~ 1.449 V versus RHE). It is important to note that the onset potentials are values taken at low currents. In addition to showing the lowest onset potential for OER, the iridium electrode also attains the highest current density and holds the lowest overpotential at 10 mA cm^{-2} , as shown in Table 2. Among the Ni-based electrocatalysts, the Ni electrode shows the highest current density, while the $\text{Ni}_{90}\text{Fe}_{10}/\text{CeO}_2$ sample exhibits the lowest onset potential for the OER at ~ 0.553 V (~ 1.478 V versus RHE). However, the $\text{Ni}_{90}\text{Fe}_{10}$ sample is the only sample that shows a lowered onset potential, while also attaining a high current density for OER. Additionally, it showed the second lowest overpotential at 10 mA cm^{-2} . From the CV shown in Figure 6b, the reaction overpotentials for OER in 0.1 M KOH can be written as $\eta_{\text{Ir black}} < \eta_{\text{Ni}_{90}\text{Fe}_{10}/\text{CeO}_2} < \eta_{\text{Ni}_{90}\text{Fe}_{10}} < \eta_{\text{Ni}}$, where the onset potential for OER or Ir occurs at ~ 0.589 V (1.455 V versus RHE). Although the Ir black still showed the lowest onset potential for the OER in 0.1 M KOH, the catalyst performs rather poorly due to apparently slow kinetics, reaching less than 5 mA cm^{-2} . The $\text{Ni}_{90}\text{Fe}_{10}$ sample, on the other hand, continued to show a relatively high current for OER and held an overpotential of 0.404 V at 5 mA cm^{-2} . The $\text{Ni}_{90}\text{Fe}_{10}/\text{CeO}_2$ sample still exhibits the lowest onset potential amongst the Ni-based materials at around 0.635 V (1.501 V versus RHE). Figure 6c,d shows Tafel plots obtained from linear sweep voltammograms (LSVs) run at 1 mV s^{-1} in the OER region. Delineated on the figures are the regions in which the slopes tabulated in Table 2 were calculated. Note that no activity coefficients or exchange current densities were reported, as accurate estimations of a complete kinetic model require very detailed studies, such as the one reported by Reksten et al. [45] for $\text{Ir}_x\text{Ru}_{(1-x)}\text{O}_2$ catalysts in acidic electrolyte.

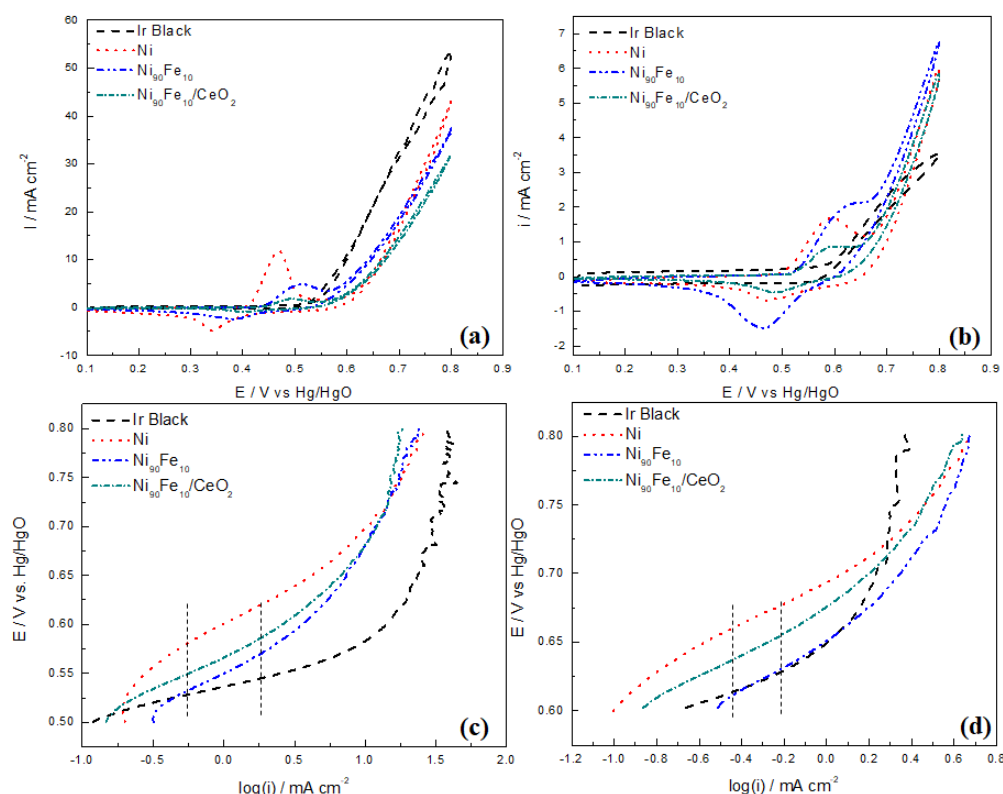


Figure 6. (a,b) Stable CVs run at 20 mV s^{-1} in 1 M and 0.1 M KOH, respectively. (c,d) Tafel plots obtained from LSVs run between $[0.3, 0.8]$ V at 1 mV s^{-1} in 1 M and 0.1 M KOH, respectively. Catalysts: Ir black (black), Ni (red), $\text{Ni}_{90}\text{Fe}_{10}$ (blue) and $\text{Ni}_{90}\text{Fe}_{10}/\text{CeO}_2$ (green) NPs.

Table 2. Tafel slopes and overpotentials at 0.1 and 1 M for Ir black, Ni, Ni₉₀Fe₁₀ and Ni₉₀Fe₁₀/CeO₂ NPs.

Catalyst	KOH Conc. [M]	Tafel Slope [mV dec ⁻¹]	η @ 5 mA cm ⁻² [mV]	η @ 10 mA cm ⁻² [mV]
Ir Black	1.0	32.0	268	295
	0.1	70.6	N/A	N/A
Ni	1.0	75.5	337	365
	0.1	73.1	424	N/A
Ni ₉₀ Fe ₁₀	1.0	71.9	298	341
	0.1	83.3	404	N/A
Ni ₉₀ Fe ₁₀ /CeO ₂	1.0	70.7	323	369
	0.1	82.1	424	N/A

The results summarized in Figure 6 and Table 2 indicate that the unsupported Ni₉₀Fe₁₀ catalyst is the most promising Ni-based material for OER in alkaline environment, as it shows both a lower onset potential and a higher current density in both 1 M and 0.1 M KOH. Amongst all Ni-based materials, it also shows the lowest overpotential at both 5 and 10 mA cm⁻². Similar results have been previously reported, where the addition of Fe increases the OER activity [18,21,23,46,47]. Increased OER overpotentials with decreasing electrolyte concentrations have also been reported [18,21,23,46,47]. When comparing values in Table 2, it is possible to observe that in this case, our Ni-based catalysts experience an increase in overpotential between 87 and 101 mV, when decreasing the electrolyte concentration from 1 M to 0.1 M KOH. As for the OER kinetics, it was noticed that the Tafel slopes obtained in 1 M KOH for our study were sometimes twice as high compared to the values reported in literature [18,20,21,23,46–48]. Discrepancies in the literature are common, with reported values ranging between 40 and 130 mV dec⁻¹ for the Tafel slope of nickel-based oxides, and are likely combinations of the regions of LSV used to calculate the slope; it is well known that there are generally two Tafel regions for OER, separated at ~1.5 V versus RHE (~0.575 V versus Hg/HgO in 1 M KOH) [17]. Another possible cause for the different Tafel slopes for Ni-based materials could be the state of the oxide surface at the time of the measurement or the scan rate selected.

In addition, only a small increase in the Tafel slope was observed for the Ni-based catalysts when decreasing the electrolyte concentration, a clear indication that the kinetics for the OER remain unchanged in this pH region. On the other hand, it seems as though the kinetics of Ir-based catalysts are considerably more affected by the decrease in KOH concentration, more than doubling the Tafel slope from 32 to 70 mV dec⁻¹, while going from 1 M to 0.1 M KOH, respectively. These results are concurrent with observations reported in literature where Ir electrodes show a rather significant decrease in performance with decreasing electrolyte pH, either due to the development of a poorly conducting oxide film on the surface of the iridium working electrode [49], a change in OER mechanism [49] or possible blocking of the electrode surface due to evolving oxygen [50]. However, Pi et al. [51] reported Tafel slopes of 32.7, 38.4 and 40.1 mV dec⁻¹ in 1 M KOH, and 42.1, 48.5, 50.2 mV dec⁻¹ in 0.1 M KOH for surface-cleaned 3D Ir nanosheets, 3D Ir nanosheets and Ir NPs, respectively. The 3D nanosheets were prepared with the wet-chemical synthesis method. A study by Lyons et al. [50] also reported similar Tafel slopes of 44 and 43 mV dec⁻¹ in 0.1 and 1 M KOH, respectively, for IrO₂ electrodes prepared via thermal decomposition onto a substrate. Finally, Tahir et al. [52], reported a Tafel slope of 65 mV dec⁻¹ in 1 M KOH for IrO₂.

Figure 6 and Table 2 show that the Ni₉₀Fe₁₀/CeO₂ catalyst has a comparable overpotential for OER to those of the unsupported Ni-based materials. Although the current is not as high when including the ceria support, the material still shows promising activity through its Tafel parameters, which are very similar to the rest of the Ni-based materials. It is important to note that the CVs presented in Figure 6 were normalized by geometric surface area; normalizing the results by mass of metallic Ni would show that the ceria supported materials are the most promising OER catalysts, as shown in Figure 7, where the current densities normalized by geometric surface area and by mass of nickel at 0.8 V versus Hg/HgO (1.725 and 1.666 V versus RHE in 1 and 0.1 M KOH, respectively), are compared. Based on the interesting

results of the cerium-content optimization reported in the paper by Chen et al. [34], future work on the Ni-based materials should include support content optimization of the synthesized catalysts. Figure S6 in the Supplementary Information shows the normalization by mass of metal in the Ni-based samples.

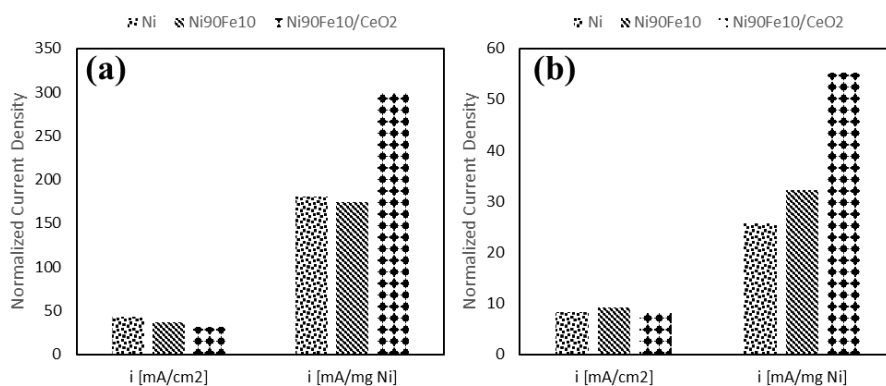


Figure 7. Comparison between current densities by geometric surface area and by mass of Ni at 0.8 V versus Hg/HgO in (a) 1 M KOH and (b) 0.1 M KOH. Data for Figure 7a,b were taken from the CVs presented in Figure 6a,b, respectively.

2.5. AEMWE Experiments

Polarization curves and electrochemical impedance spectroscopy (EIS) were carried out in an AEMWE cell. As shown in Figure 8a,b, polarization curves in 1 M KOH show a significantly higher performance and lower overpotential for OER than those taken in 0.1 M KOH. Achieving current densities of 2 A cm^{-2} at cell voltages of 1.85–1.9 V in 1 M KOH at 50°C , may be regarded as an excellent result, considering the non-noble metal nature of these catalysts [2,8]. In 1 M KOH, the Ni and Ni₉₀Fe₁₀ electrodes show similar performance to the benchmark at only twice the intended metallic loading (6 mg cm^{-2} versus 3 mg cm^{-2} for Ir-black). As shown in Table 3, the Ni₉₀Fe₁₀ and Ni₉₀Fe₁₀/CeO₂ electrodes have lower overpotentials than the Ni electrode at lower current densities; however, not at higher current densities, in accordance with our ex-situ CV experiments (Figure 6a,b). In 0.1 M KOH, the Ni₉₀Fe₁₀ electrode was the only catalyst that could reach an operating current of 2 A cm^{-2} , without inducing too high an overpotential. Contrary to the non-noble catalyst results, the Ir black benchmark electrode shows a significant decrease in performance at the lower electrolyte concentration. This result not only reflects the three-electrode cell results very nicely, but also shows that Ni-based electrocatalysts, particularly the Ni₉₀Fe₁₀ catalyst, are promising electrocatalysts for use as AEMWE anodes. The Ni₉₀Fe₁₀ catalyst shows similar performance as the Ir noble metal in 1 M KOH and outperforms the noble metal in 0.1 M. The nickel-based materials in this work also show comparable, if not better, performance than other AEMWE tests carried out with similar set ups [12,53].

EIS measurements were carried out to evaluate the overall cell resistance and charge transfer resistance for the single AEMWE cell. Figure 8c,d and Table 3 show the EIS of each cell set up at 1 A cm^{-2} . Although the EIS measurements were done for the full cell, a simple R(QR) circuit was used to fit the experimental data. The R(QR) model is shown in the corners of Figure 8c,d, and consists of a solution or overall cell resistance (R_{EL}) in series with a parallel combination of a charge transfer resistance (R_{CT}) and a constant phase element (Q). R_{EL} is found from the high frequency intersection of the real axis of the fitted curve, while the R_{CT} is represented by the diameter of the ensuing semicircle. All parameters were extracted from fits of the experimental data and reproduced in Table 3 under various conditions. Apart from the Ni₉₀Fe₁₀/CeO₂, all anodes exhibited similar R_{EL} in 1 M KOH. As the R_{EL} corresponds to the ohmic resistance of the cell, it was expected that it be similar for the unsupported Ni, Ir and Ni₉₀Fe₁₀ catalysts. It is interesting to observe that the electrolyser cell using the Ni₉₀Fe₁₀/CeO₂ shows more than twice the R_{EL} compared to the other cells for the same KOH concentration. This increase in ohmic resistance is caused by the rather large amount of less-conductive ceria in the catalytic layer (6 mg cm^{-2} for both the Ni catalyst and the CeO₂ support), increasing the thickness of the catalytic layer. Incorporating ceria into

the catalyst therefore affected both the electrode bulk conductivity and contact resistance between the anode electrode and the porous transport layers (PTLs). Nevertheless, the $\text{Ni}_{90}\text{Fe}_{10}/\text{CeO}_2$ anode showed lower charge-transfer resistances in both 0.1 and 1 M KOH, indicating good kinetics.

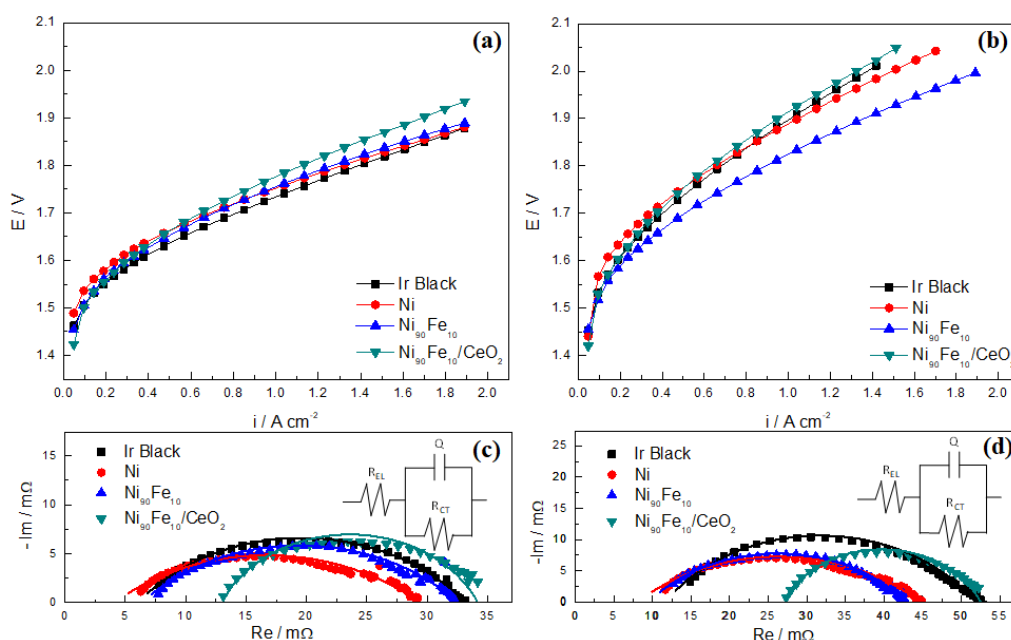


Figure 8. (a,b) Polarization curves up to 2 A cm^{-2} in 1 M and 0.1 M KOH, respectively. (c,d) Electrochemical impedance spectroscopy in 1 M and 0.1 M KOH, respectively. Catalysts: Ir black (black square), Ni (red circle), $\text{Ni}_{90}\text{Fe}_{10}$ (blue triangle) and $\text{Ni}_{90}\text{Fe}_{10}/\text{CeO}_2$ (green inverted triangle) NPs. Experiments were conducted at $50 \text{ }^\circ\text{C}$.

Table 3. Summary of polarization curve and electrochemical impedance results.

Catalyst.	KOH conc. [M]	$E @ 0.4 \text{ A/cm}^2$ [V]	$E @ 1.4 \text{ A/cm}^2$ [V]	R_{EL} [mΩ]	R_{CT} [mΩ]	$Y [10^{-4} \text{ F s}^{(1-\alpha)}]$	α
Ir Black	1.0	1.608	1.804	6.0 ± 0.1	27 ± 0.1	3.6 ± 0.1	0.577 ± 0.005
	0.1	1.691	2.011	11.6 ± 0.2	40.2 ± 0.3	11.5 ± 0.1	0.618 ± 0.007
Ni	1.0	1.636	1.815	4.1 ± 0.2	25.2 ± 0.3	12.8 ± 0.8	0.465 ± 0.009
	0.1	1.713	1.984	8.0 ± 0.3	36.7 ± 0.5	6.4 ± 0.4	0.478 ± 0.009
$\text{Ni}_{90}\text{Fe}_{10}$	1.0	1.622	1.823	6.3 ± 0.2	26.1 ± 0.3	6.6 ± 0.5	0.53 ± 0.01
	0.1	1.659	1.911	9.4 ± 0.1	33.6 ± 0.2	2.8 ± 0.1	0.551 ± 0.005
$\text{Ni}_{90}\text{Fe}_{10}/\text{CeO}_2$	1.0	1.627	1.854	13.0 ± 0.4	21.2 ± 0.2	10.1 ± 0.3	0.74 ± 0.04
	0.1	1.703	2.023	27.0 ± 0.4	25.6 ± 0.6	0.5 ± 0.1	0.74 ± 0.02

Table 3 clearly shows that decreasing that the KOH concentration decreases electrolysis performance for all materials by affecting the charge transfer resistance (R_{CT}) and kinetics of the electrochemical reactions, and the ohmic resistance or electrolyte resistance (R_{EL}) through a lack of OH^- ions. However, in the case of the $\text{Ni}_{90}\text{Fe}_{10}$ and $\text{Ni}_{90}\text{Fe}_{10}/\text{CeO}_2$, the decrease in KOH concentration does not have as large an effect on the activity and kinetics of the OER compared to the Ni and Ir catalysts. The presence of Fe in the catalysts seems to shift the OER onset potential to lower values due to the formation of a NiFe mixed oxyhydroxide ($\text{Ni}_x\text{Fe}_{(1-x)}\text{OOH}$) independent of pH [25].

3. Materials and Methods

3.1. Synthesis of Ni-Based Materials by Chemical Reduction

Ni, $\text{Ni}_{90}\text{Fe}_{10}$ and $\text{Ni}_{90}\text{Fe}_{10}/\text{CeO}_2$ nanoparticles (NPs) were synthesized by a scalable chemical reduction method in ethanol using sodium borohydride as the reducing agent. First, the nickel chloride

hexahydrate ($\text{NiCl}_2 \cdot 6\text{H}_2\text{O}$, 99.999% purity, Sigma Aldrich, St. Louis, MO, USA) precursor salt was dissolved in ethanol (EtOH, 99%, Greenfield, Grayslake, IL, USA) with magnetic stirring for 45 min at room temperature. Depending on whether the desired compound included Fe or CeO_2 , or both, the ferrous sulphate heptahydrate ($\text{FeSO}_4 \cdot 7\text{H}_2\text{O}$, $\geq 99\%$, Sigma Aldrich, St. Louis, MO, USA), precursor salt and cerium oxide nanopowder support (CeO_2 , 99.5%, Alfa Aesar, Haverhill, MA, USA) were dissolved in ethanol using the same procedure. Next, the solutions were mixed together, and magnetic stirring was continued for 5 min to ensure that the solution was homogenous. Sodium borohydride (NaBH_4 , $\geq 98\%$, ACROS, Geel, Belgium) was then dissolved in around 5–10 mL of ultrapure water (ultrapure water, Milli-Q[®] Millipore, 18.2 M Ω cm at 293 K), then added to the reaction mixture, which was then further mixed for 30 min to ensure everything was completely reduced. Once the reaction was complete, the nanoparticles were washed three times with ethanol using a centrifuge run at 6000 rpm for 10 min per wash. Finally, the particles were left in a freeze drier overnight (around 15 h) to remove all residual ethanol from the sample. In this study, monometallic Ni nanoparticles were prepared, as were $\text{Ni}_{90}\text{Fe}_{10}$ (at%) and $\text{Ni}_{90}\text{Fe}_{10}/\text{CeO}_2$ (50 wt% $\text{Ni}_{90}\text{Fe}_{10}$ metal supported on CeO_2). Note that all glassware used in the NP synthesis was cleaned using the Aqua Regia procedure (2:1 HCl: HNO_3 , 37%, 70%, respectively, Sigma Aldrich, St. Louis, MO, USA). This synthesis procedure was easily scaled by adjusting the precursor salt quantities for the new desired material output, and by modifying the ethanol required to dissolve the salts. This ensured a similar concentration of precursor salts throughout all batches.

3.2. Material Characterization

The transmission electron microscopy (TEM) micrographs for the Ni and $\text{Ni}_{90}\text{Fe}_{10}$ catalysts were taken on the JEOL JEM 2100F Field Emission Transmission Electron Microscope (FETEM) (Tokyo, Japan) with an operating voltage of 200 kV. The scanning electron microscopy (SEM) micrographs of all AEMWE anodes were taken on the Hitachi Model S-3400N PC-Based Variable Pressure Scanning Electron Microscope (ON, Canada). SEM images were taken at an acceleration voltage of 15 kV. X-ray diffraction (XRD) results for the Ni and $\text{Ni}_{90}\text{Fe}_{10}$ catalysts were measured using the Rigaku Ultima IV multi-purpose diffractometer (Tokyo, Japan) using Copper $\text{K}\alpha$ radiation and an x-ray wave length λ , of 1.5418 Å, at 40 kV and 44 mA. The XRD spectra were taken over a 2θ range of 20° – 80° at a rate of $0.5^\circ 2\theta \text{ min}^{-1}$.

For the $\text{Ni}_{90}\text{Fe}_{10}/\text{CeO}_2$ material an Field Electron and Ion Company (FEI, Hillsboro, OR, USA) Titan3 80–300 TEM operated at 300 keV, equipped with a corrected electron optical systems (CEOS) aberration corrector for the probe forming lens and a monochromated field-emission gun, was used to obtain both high-resolution TEM (HRTEM) and annular dark-field (ADF) images. The ADF images were collected using a high-angle annular dark-field (HAADF) Fischione detector in the scanning transmission electron microscopy (STEM) mode. Additionally, energy-dispersive X-ray (EDX) spectroscopy and electron energy-loss spectroscopy (EELS) were carried out on the ceria-supported material using the TEM instrument described above, equipped with an EDX spectrometer (EDAX Analyzer, DPP-II) and an EELS spectrometer with a Gatan Tridiem 866 Image Filter. To optimize the signal intensity, EDX spectra were acquired with the specimen tilted at 15 degrees. EELS spectra were acquired in STEM with a convergence semi angle of 15 mrad and an acceptance semi angle of 40 mrad. Techniques not presented in the main article are presented in the Supplementary Information.

3.3. Ex-Situ Experiments

3.3.1. Cell Set-Up

The synthesized materials were first studied for the OER in a conventional, two-compartment, three-electrode electrochemical glass cell. The working and counter electrodes (WE and CE) were in the main compartment, while the reference electrode (RE) was in the second compartment. Prior to experiments, the glassy carbon surface of the WE was first polished with 30 micron alumina (Al_2O_3 ,

Carveth Metallurgical Limited, Canada), then with 3 micron alumina (Al_2O_3 , Buehler, Lake Bluff, IL, USA), both of which were mixed with ultrapure water. After polishing, the electrode surface was wiped with ethanol, then ultrapure water. The WE consisted of 10 μL of a catalyst ink deposited on a 0.196 cm^2 glassy carbon electrode. The catalyst ink was made with 6 mg catalyst, 1 mL of ultrapure water, 200 μL isopropanol (IPA, 99.9%, Fischer Scientific, Hampton, NH, USA) and 100 μL of Nafion[®] (~5%, Sigma Aldrich, St. Louis, MO, USA). Once the ink was made, it was sonicated for around 5 min, then the deposited ink was dried in an oven at 60 °C. The CE was a platinum mesh and the RE was mercury/mercury oxide (Hg/HgO) electrode (Koslow Scientific Company, Englewood, NJ, USA). Note that all potentials in this article are reported with respect to the Hg/HgO reference electrode unless otherwise specified. See the Supplementary Information for conversions to RHE and how the overpotentials were calculated. All electrochemistry experiments were carried out using either 1 M or 0.1 M potassium hydroxide solutions (KOH, $\geq 85\%$, Sigma Aldrich, St. Louis, MO, USA) at a room temperature of around 23 °C.

3.3.2. OER Experiments

Electrochemical tests were conducted using the Bio-Logic Potentiostat/Galvanostat using the EC Labs software (Bio-Logic Science Instruments, Seyssinet-Pariset, France). The OER tests included a cyclic voltammogram (CV) run between [0.1, 0.8] V for 10 cycles at a scan rate of 20 mV s^{-1} , followed by a linear sweep voltammogram (LSV) run between [0.3, 0.8] V at a scan rate of 1 mV s^{-1} . The tests mentioned were applied to the nickel-based materials, and an iridium black benchmark (Ir black, 99.8%, Alfa Aesar, Haverhill, MA, USA) catalyst. Before running the CVs and LSVs on the Ni-based materials, the WEs were polarized at -1.3 V for 5 min, and -0.8 V for 10 min [54], to first remove the oxides from the surfaces, and then to remove the hydrogen produced in the first polarization step. Only the fifth cycle of all cyclic voltammetry experiments is reported.

3.4. In Situ Experiments

3.4.1. Cell Set-Up

The AEMWE cell hardware consisted of a modified 25 cm^2 fuel cell hardware (BalticFuelCell GmbH). The cell has parallel flow fields made with gold coated titanium, which were used as both anode and cathode endplates. The endplate material selection was based on minimizing ohmic losses in the AEMWE cell or rather to minimize the interfacial contact resistances (ICRs). The electrolyser setup also included a 5 L Teflon tank with heaters, which was used as the KOH reservoir. A double headed peristaltic pump was used to pump 300 mL min^{-1} of KOH through the AEMWE cell at both anode and cathode.

The membrane electrode assembly consisted of a commercial anionic exchange membrane (fumasep FAA-3PE-30, Fumatech, Bietigheim-Bissingen, Germany), onto which the anode and cathode were hand-sprayed with an air brush. The membrane was secured with a gasket, as shown in Figure 9. Furthermore, in the interest of conserving material, only 5 cm^2 of the 25 cm^2 cell was used for the electrode area. The MEAs were assembled in the cell between two, 1 mm thick, commercially available, titanium, porous transport layers (PTLs) (Bekaert, Zwevegem, Belgium).

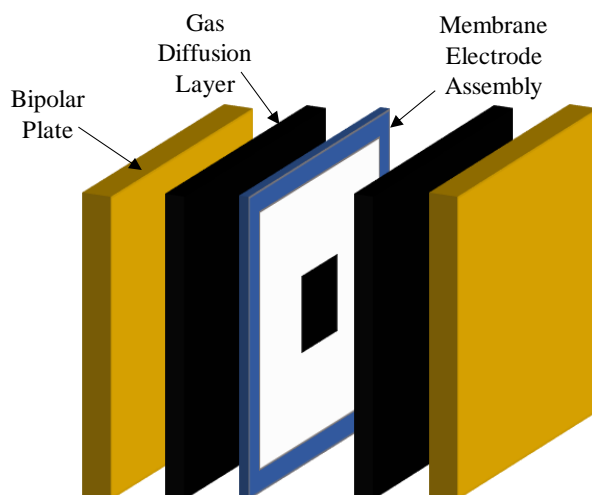


Figure 9. Compact Alkaline Exchange Membrane Water Electrolyser Cell Design.

The anodes consisted of the previously mentioned Ni-based materials, and the Ir-black benchmark (Alfa Aesar, City, Haverhill, MA, USA), while the cathode consisted of platinum supported on carbon (Pt/C, 60 wt% metal on support, Alfa Aesar, Haverhill, MA, USA). The ink for the anodes were made with a solution of 50:50 by weight of ultrapure water: IPA, which included ~2 wt% metal and an anionic ionomer (fumion FAA-3-SOLUT-10, Bietigheim-Bissingen, Fumatech, Germany). The final electrode had ~10 wt% ionomer acting as both a catalyst binder and a facilitator for hydroxide ion transport. Multiple sonication and ultrasonication steps were used to ensure the solution was very fine and well dispersed. The ink for the cathodes were made in a similar way to the anode inks; however, the ionomer was present at ~23 wt% in the final electrode. Note that the ink preparation procedures were obtained by ink optimization of the benchmark electrodes; namely, the Ir-black anode and the Pt/C cathode.

In the AEMWE experiments, the anode loading for the benchmark was 3 mg cm^{-2} , while the loading for the Ni-based materials was 6 mg cm^{-2} . The cathode loading was held at a Pt loading of 1 mg cm^{-2} for all experiments. Note that those are intended metal loadings. For the actual metal loadings, see Table S1 in the Supplementary Information of this article. Actual metal loadings were calculated using ImageJ and a differential weight of samples taken from the template used to delimit the electrode area during spraying.

3.4.2. AEMWE Experiments

Before starting electrolysis testing, the cell was mounted into the system, and around 2 L of 1 M KOH was circulated through the system overnight to exchange the bromine anions in the membrane with hydroxide ions from the alkaline electrolyte. The system was then cleaned by pumping ultrapure water through it. Electrolysis testing was then carried out using the HCP-803 Potentiostat equipped with the EC Labs software (Bio-Logic Science Instruments, Seyssinet-Pariset, France). First, polarization curves were taken, by stepping up the current from 0 to 10 A (0 to 2 A cm^{-2}). Next, electrochemical impedance spectroscopy (EIS) was performed by applying a direct current (DC) of 5 A (1 A cm^{-2}) and an alternating current (AC) of $\pm 5\%$ DC, while the frequency ranged from 20,000 to 0.1 Hz. The impedance data was fitted to a simple equivalent circuit using magnitude weighting in the Maple application “Complex Nonlinear Least Squares Fitting of Immittance Data,” authored by David Harrington [55]. Polarization and EIS experiments were repeated three times in 1 M KOH, after which the system was flushed with ultrapure water, then all measurements were taken three times in 0.1 M KOH. All AEMWE experiments were performed at $50 \pm 2 \text{ }^\circ\text{C}$, by controlling the temperature in the cell and the KOH storage tank, individually.

4. Conclusions

In this study, Ni-based materials were synthesized for the promotion of the oxygen evolution reaction for applications in energy storage through anion-exchange, membrane-alkaline water electrolysis (AEMWE). Ni, Ni₉₀Fe₁₀ and Ni₉₀Fe₁₀/CeO₂ NPs were synthesized via chemical reduction in ethanol using sodium borohydride. The materials were characterized by TEM imaging and were found to be around 4–6 nm in size. Ex-situ electrochemical experiments were conducted in a conventional three-electrode cell at both 1 M and 0.1 M KOH and results were compared to an Ir-black benchmark electrode. Results indicate that on average, the Ni₉₀Fe₁₀ material is the best-performing material for OER, showing very low onset potentials and excellent catalytic activity. This result was also obtained for the lower electrolyte concentration, wherein the NiFe-based electrode outperformed all catalysts, including the Ir benchmark electrode.

In-situ AEMWE experiments were performed in a modified 25 cm² fuel cell for simultaneous O₂ and H₂ production. At twice the metallic loading compared to the Ir benchmark anode, the Ni-based materials showed state-of-the-art performance, achieving current densities of 2 A cm⁻² at 1.85–1.9 V in 1 M KOH at 50 °C. In 0.1 M KOH, the cell set up using the Ni₉₀Fe₁₀ anode attained 1.99 V at 2 A cm⁻². These are promising results, considering the non-noble metal nature of these catalysts and that long-term stability measurements are on-going. Based on impedance results, the ceria-supported NiFe catalyst showed higher cell resistances (higher R_{EL} values), yet showed a low onset potential for the OER, and a low charge transfer resistance, indicating the Ni₉₀Fe₁₀/CeO₂ may be used as an anode catalyst in AEMWE if the support is further optimized in terms of electrical conductivity.

Supplementary Materials: The following are available online at <http://www.mdpi.com/2073-4344/9/10/814/s1>, Figure S1: CVs from 0.1 to 0.8 V of Ni (black), CeO₂ (red) and Ni/CeO₂ (blue) run at 20 mV s⁻¹ in 1 M KOH. Figure S2: TEM Images of Ni₉₀Fe₁₀/CeO₂ showing (a) mostly the Ni and Fe and (b) mostly the CeO₂ support. Figure S3: STEM Images of Ni₉₀Fe₁₀/CeO₂ showing (a) mostly the Ni and Fe and (b) mostly the CeO₂ support. Figure S4: Spatially-resolved EDX of Ni₉₀Fe₁₀/CeO₂. (a) Shows the two selected regions of the STEM image, (b) shows the analysis of Region 1 and (c) shows the analysis of Region 2. Figure S5: EELS mapping of Ni₉₀Fe₁₀/CeO₂. (a) Shows the Fe mapping, (b) shows the Ni mapping and (c) shows the analyzed region in orange. Figure S6: Comparison between current densities by geometric surface area and by mass of metal at 0.8 V against Hg/HgO in (a) 1 M KOH and (b) 0.1 M KOH. Table S1: Anode metal loadings on the membrane electrode assemblies.

Author Contributions: Material synthesis, characterization, ex-situ oxygen evolution measurements, in-situ electrolysis measurements, writing and editing, E.C. In-situ electrolysis measurements, funding acquisition, supervision, writing and editing, A.O.B. Funding acquisition, supervision, writing and editing, F.S. funding acquisition, supervision, writing and editing, E.A.B.

Funding: This research was conducted as part of the Engineered Nickel Catalysts for Electrochemical Clean Energy project administered from Queen's University and supported by Grant number RGPNM 477963-2015 under the Natural Sciences and Engineering Research Council of Canada (NSERC) Discovery Frontiers Program. Additionally, this work was performed within the HAPEEL project "Hydrogen Production by Alkaline Polymer Electrolyte Electrolysis," financially supported by the Research Council of Norway-ENERGIX program, contract number 268019. The Research Council of Norway is also acknowledged for the support to the Norwegian Fuel cell and Hydrogen Centre and the INTPART project 261620.

Acknowledgments: The authors would also like to thank Martin Couillard from the Natural Research Council of Canada for his help in characterizing the Ni₉₀Fe₁₀/CeO₂ sample.

Conflicts of Interest: The authors declare no conflict of interest.

References

1. Clark, D.; Brandon, N. *What's the "Hydrogen Economy"?* The Guardian: London, UK, 2012.
2. Zeng, K.; Zhang, D. Recent progress in alkaline water electrolysis for hydrogen production and applications. *Prog. Energy Combust. Sci.* **2010**, *36*, 307–326. [[CrossRef](#)]
3. Leng, Y.; Chen, G.; Mendoza, A.J.; Tighe, T.B.; Hickner, M.A.; Wang, C.Y. Solid-state water electrolysis with an alkaline membrane. *J. Am. Chem. Soc.* **2012**, *134*, 9054–9057. [[CrossRef](#)] [[PubMed](#)]
4. Varcoe, J.R.; Atanassov, P.; Dekel, D.R.; Herring, A.M.; Hickner, M.A.; Kohl, P.A.; Kucernak, A.R.; Mustain, W.E.; Nijmeijer, K.; Scott, K.; et al. Anion-exchange membranes in electrochemical energy systems. *Energy Environ. Sci.* **2014**, *7*, 3135–3191. [[CrossRef](#)]

5. Cho, M.K.; Park, H.Y.; Lee, H.J.; Kim, H.J.; Lim, A.; Henkensmeier, D.; Yoo, S.J.; Kim, J.Y.; Lee, S.Y.; Park, H.S.; et al. Alkaline anion exchange membrane water electrolysis: Effects of electrolyte feed method and electrode binder content. *J. Power Sources* **2018**, *382*, 22–29. [[CrossRef](#)]
6. Vincent, I.; Bessarabov, D. Low cost hydrogen production by anion exchange membrane electrolysis: A review. *Renew. Sustain. Energy Rev.* **2018**, *81*, 1690–1704. [[CrossRef](#)]
7. Phillips, R.; Edwards, A.; Rome, B.; Jones, D.R.; Dunnill, C.W. Minimising the ohmic resistance of an alkaline electrolysis cell through effective cell design. *Int. J. Hydrog. Energy* **2017**, *42*, 23986–23994. [[CrossRef](#)]
8. Park, J.E.; Kang, S.Y.; Oh, S.H.; Kim, J.K.; Lim, M.S.; Ahn, C.Y.; Cho, Y.H.; Sung, Y.E. High-performance anion-exchange membrane water electrolysis. *Electrochim. Acta* **2019**, *295*, 99–106. [[CrossRef](#)]
9. Hnát, J.; Paidar, M.; Schauer, J.; Žitka, J.; Bouzek, K. Polymer anion-selective membranes for electrolytic splitting of water. Part II: Enhancement of ionic conductivity and performance under conditions of alkaline water electrolysis. *J. Appl. Electrochem.* **2012**, *42*, 545–554. [[CrossRef](#)]
10. Chanda, D.; Hnát, J.; Bystron, T.; Paidar, M.; Bouzek, K. Optimization of synthesis of the nickel-cobalt oxide based anode electrocatalyst and of the related membrane-electrode assembly for alkaline water electrolysis. *J. Power Sources* **2017**, *347*, 247–258. [[CrossRef](#)]
11. Kim, J.H.; Lee, J.N.; Yoo, C.Y.; Lee, K.B.; Lee, W.M. Low-cost and energy-efficient asymmetric nickel electrode for alkaline water electrolysis. *Int. J. Hydrog. Energy* **2015**, *40*, 10720–10725. [[CrossRef](#)]
12. Schalenbach, M.; Kasian, O.; Mayrhofer, K.J.J. An alkaline water electrolyzer with nickel electrodes enables efficient high current density operation. *Int. J. Hydrog. Energy* **2018**, *43*, 11932–11938. [[CrossRef](#)]
13. Liu, Z.; Sajjad, S.D.; Gao, Y.; Yang, H.; Kaczur, J.J.; Masel, R.I. The effect of membrane on an alkaline water electrolyzer. *Int. J. Hydrog. Energy* **2017**, *42*, 29661–29665. [[CrossRef](#)]
14. Katsounaros, I.; Cherevko, S.; Zeradjanin, A.R.; Mayrhofer, K.J.J. Oxygen electrochemistry as a cornerstone for sustainable energy conversion. *Angew. Chem. Int. Ed.* **2014**, *53*, 102–121. [[CrossRef](#)] [[PubMed](#)]
15. Marini, S.; Salvi, P.; Nelli, P.; Pesenti, R.; Villa, M.; Berrettoni, M.; Zangari, G.; Kiros, Y. Advanced alkaline water electrolysis. *Electrochim. Acta* **2012**, *82*, 384–391. [[CrossRef](#)]
16. Faid, A.; Oyarce Barnett, A.; Seland, F.; Sunde, S. Highly active nickel-based catalyst for hydrogen evolution in anion exchange membrane electrolysis. *Catalysts* **2018**, *8*, 614. [[CrossRef](#)]
17. Fabbri, E.; Haberer, A.; Waltar, K.; Kötz, R.; Schmidt, T.J. Developments and perspectives of oxide-based catalysts for the oxygen evolution reaction. *Catal. Sci. Technol.* **2014**, *4*, 3800–3821. [[CrossRef](#)]
18. Li, X.; Walsh, F.C.; Pletcher, D. Nickel based electrocatalysts for oxygen evolution in high current density, alkaline water electrolyzers. *Phys. Chem. Chem. Phys.* **2011**, *13*, 1162–1167. [[CrossRef](#)] [[PubMed](#)]
19. Cho, M.K.; Lim, A.; Lee, S.Y.; Kim, H.; Yoo, S.J.; Sung, Y.; Park, H.S.; Jang, J.H. A review on membranes and catalysts for anion exchange membrane water electrolysis single cells. *J. Electrochem. Sci. Technol.* **2017**, *8*, 183–196. [[CrossRef](#)]
20. Trotochaud, L.; Ranney, J.K.; Williams, K.N.; Boettcher, S.W. Solution-cast metal oxide thin film electrocatalysts for oxygen evolution. *J. Am. Chem. Soc.* **2012**, *134*, 17253–17261. [[CrossRef](#)] [[PubMed](#)]
21. Gong, M.; Dai, H. A mini review of NiFe-based materials as highly active oxygen evolution reaction electrocatalysts. *Nano Res.* **2015**, *8*, 23–39. [[CrossRef](#)]
22. Long, X.; Ma, Z.; Yu, H.; Gao, X.; Pan, X.; Chen, X.; Yang, S.; Yi, Z. Porous FeNi oxide nanosheets as advanced electrochemical catalysts for sustained water oxidation. *J. Mater. Chem. A* **2016**, *4*, 14939–14943. [[CrossRef](#)]
23. Gong, M.; Li, Y.; Wang, H.; Liang, Y.; Wu, J.Z.; Zhou, J.; Wang, J.; Regier, T.; Wei, F.; Dai, H. An advanced Ni-Fe layered double hydroxide electrocatalyst for water oxidation. *J. Am. Chem. Soc.* **2013**, *135*, 8452–8455. [[CrossRef](#)] [[PubMed](#)]
24. Bode, H.; Dehmelt, K.; White, J. Zur kenntnis der nickelhydroxidelektrode—I.Über das nickel (II)-hydroxidhydrat. *Electrochim. Acta* **1966**, *11*, 1079–1087. [[CrossRef](#)]
25. Diaz-Morales, O.; Ferrus-Suspedra, D.; Koper, M.T.M. The importance of nickel oxyhydroxide deprotonation on its activity towards electrochemical water oxidation. *Chem. Sci.* **2016**, *7*, 2639–2645. [[CrossRef](#)] [[PubMed](#)]
26. Surendranath, Y.; Kanan, M.W.; Nocera, D.G. Mechanistic studies of the oxygen evolution reaction by a cobalt-phosphate catalyst at neutral pH. *J. Am. Chem. Soc.* **2010**, *132*, 16501–16509. [[CrossRef](#)] [[PubMed](#)]
27. Takashima, T.; Hashimoto, K.; Nakamura, R. Mechanisms of pH-dependent activity for water oxidation to molecular oxygen by MnO₂ electrocatalysts. *J. Am. Chem. Soc.* **2012**, *134*, 1519–1527. [[CrossRef](#)] [[PubMed](#)]

28. Lyons, M.E.G.; Cakara, A.; O'Brien, P.; Godwin, I.; Doyle, R.L. Redox, pH sensing and electrolytic water splitting properties of electrochemically generated nickel hydroxide thin films in aqueous alkaline solution. *Int. J. Electrochem. Sci.* **2012**, *7*, 11768–11795.
29. Lyons, M.E.G.; Doyle, R.L.; Brandon, M.P. Redox switching and oxygen evolution at oxidized metal and metal oxide electrodes: Iron in base. *Phys. Chem. Chem. Phys.* **2011**, *13*, 21530–21551. [[CrossRef](#)]
30. Panaritis, C.; Edake, M.; Couillard, M.; Einakchi, R.; Baranova, E.A. Insight towards the role of ceria-based supports for reverse water gas shift reaction over RuFe nanoparticles. *J. CO₂ Util.* **2018**, *26*, 350–358. [[CrossRef](#)]
31. Dole, H.A.E.; Baranova, E.A. Ethylene oxidation in an oxygen-deficient environment: Why ceria is an active support? *ChemCatChem* **2016**, *8*, 1977–1986. [[CrossRef](#)]
32. Rao, G.R.; Mishra, B.G. Structural redox and catalytic chemistry of ceria based materials. *Bull. Catal. Soc. India* **2003**, *2*, 122–134.
33. Feng, J.-X.; Ye, S.-H.; Xu, H.; Tong, Y.-X.; Li, G.-R. Design and synthesis of FeOOH/CeO₂ heterolayered nanotube electrocatalysts for the oxygen evolution reaction. *Adv. Mater.* **2016**, *28*, 4698–4703. [[CrossRef](#)] [[PubMed](#)]
34. Chen, Z.; Kronawitter, C.X.; Yang, X.; Yeh, Y.W.; Yao, N.; Koel, B.E. The promoting effect of tetravalent cerium on the oxygen evolution activity of copper oxide catalysts. *Phys. Chem. Chem. Phys.* **2017**, *19*, 31545–31552. [[CrossRef](#)] [[PubMed](#)]
35. Favaro, M.; Drisdell, W.S.; Marcus, M.A.; Gregoire, J.M.; Crumlin, E.J.; Haber, J.A.; Yano, J. An operando investigation of (Ni-Fe-Co-Ce)Ox system as highly efficient electrocatalyst for oxygen evolution reaction. *ACS Catal.* **2017**, *7*, 1248–1258. [[CrossRef](#)]
36. Haber, J.A.; Cai, Y.; Jung, S.; Xiang, C.; Mitrovic, S.; Jin, J.; Bell, A.T.; Gregoire, J.M. Discovering Ce-rich oxygen evolution catalysts, from high throughput screening to water electrolysis. *Energy Environ. Sci.* **2014**, *7*, 682–688. [[CrossRef](#)]
37. McCrory, C.C.L.; Jung, S.; Peters, J.C.; Jaramillo, T.F. Benchmarking heterogeneous electrocatalysts for the oxygen evolution reaction. *J. Am. Chem. Soc.* **2013**, *135*, 16977–16987. [[CrossRef](#)] [[PubMed](#)]
38. Seetharaman, S.; Balaji, R.; Ramya, K.; Dhathathreyan, K.S.; Velan, M. Graphene oxide modified non-noble metal electrode for alkaline anion exchange membrane water electrolyzers. *Int. J. Hydrog. Energy* **2013**, *38*, 14934–14942. [[CrossRef](#)]
39. Xiao, L.; Zhang, S.; Pan, J.; Yang, C.; He, M.; Zhuang, L.; Lu, J. First implementation of alkaline polymer electrolyte water electrolysis working only with pure water. *Energy Environ. Sci.* **2012**, *5*, 7869–7871. [[CrossRef](#)]
40. Ayers, K.E.; Anderson, E.B.; Capuano, C.B.; Niedzwiecki, M.; Hickner, M.A.; Wang, C.-Y.; Leng, Y.; Zhao, W. Characterization of anion exchange membrane technology for low cost electrolysis. *ECS Trans.* **2013**, *45*, 121–130. [[CrossRef](#)]
41. Pavel, C.C.; Cecconi, F.; Emiliani, C.; Santiccioli, S.; Scaffidi, A.; Catanorchi, S.; Comotti, M. Highly efficient platinum group metal free based membrane-electrode assembly for anion exchange membrane water electrolysis. *Angew. Chem. Int. Ed.* **2014**, *53*, 1378–1381. [[CrossRef](#)] [[PubMed](#)]
42. Sun, Y.P.; Li, X.Q.; Cao, J.; Zhang, W.X.; Wang, H.P. Characterization of zero-valent iron nanoparticles. *Adv. Colloid Interface Sci.* **2006**, *120*, 47–56. [[CrossRef](#)] [[PubMed](#)]
43. Hall, D.S.; Lockwood, D.J.; Bock, C.; MacDougall, B.R. Nickel hydroxides and related materials: A review of their structures, synthesis and properties. *Proc. R. Soc. A Math. Phys. Eng. Sci.* **2015**, *471*, 20140792. [[CrossRef](#)] [[PubMed](#)]
44. Baranova, E.A.; Le Page, Y.; Ilin, D.; Bock, C.; MacDougall, B.; Mercier, P.H.J. Size and composition for 1–5 nm Ø PtRu alloy nano-particles from Cu K α X-ray patterns. *J. Alloys Compd.* **2009**, *471*, 387–394. [[CrossRef](#)]
45. Reksten, A.H.; Thuv, H.; Seland, F.; Sunde, S. The oxygen evolution reaction mechanism at Ir_xRu_{1-x}O₂ powders produced by hydrolysis synthesis. *J. Electroanal. Chem.* **2018**, *819*, 547–561. [[CrossRef](#)]
46. Lyons, M.E.G.; Brandon, M.P. A comparative study of the oxygen evolution reaction on oxidised nickel, cobalt and iron electrodes in base. *J. Electroanal. Chem.* **2010**, *641*, 119–130. [[CrossRef](#)]
47. Lu, X.; Zhao, C. Electrodeposition of hierarchically structured three-dimensional nickel-iron electrodes for efficient oxygen evolution at high current densities. *Nat. Commun.* **2015**, *6*, 6616. [[CrossRef](#)]

48. Tahir, M.; Pan, L.; Idrees, F.; Zhang, X.; Wang, L.; Zou, J.J.; Wang, Z.L. Electrocatalytic oxygen evolution reaction for energy conversion and storage: A comprehensive review. *Nano Energy* **2017**, *37*, 136–157. [[CrossRef](#)]
49. Cherevko, S.; Geiger, S.; Kasian, O.; Kulyk, N.; Grote, J.-P.; Savan, A.; Shrestha, R.B.; Merzlikin, S.; Breitbach, B.; Ludwig, A.; et al. Oxygen and hydrogen evolution reactions on Ru, RuO₂, Ir, and IrO₂ thin film electrodes in acidic and alkaline electrolytes: A comparative study on activity and stability. *Catal. Today* **2015**, *262*, 170–180. [[CrossRef](#)]
50. Lyons, M.E.G.; Floquet, S. Mechanism of oxygen reactions at porous oxide electrodes. Part 2—Oxygen evolution at RuO₂, IrO₂ and Ir_xRu_{1-x}O₂ electrodes in aqueous acid and alkaline solution. *Phys. Chem. Chem. Phys.* **2011**, *13*, 5314–5335. [[CrossRef](#)]
51. Pi, Y.; Zhang, N.; Guo, S.; Guo, J.; Huang, X. Ultrathin laminar Ir superstructure as highly efficient oxygen evolution electrocatalyst in broad pH range. *Nano Lett.* **2016**, *16*, 4424–4430. [[CrossRef](#)]
52. Tahir, M.; Mahmood, N.; Zhang, X.; Mahmood, T.; Butt, F.K.; Aslam, I.; Tanveer, M.; Idrees, F.; Khalid, S.; Shakir, I.; et al. Bifunctional catalysts of Co₃O₄@GCN tubular nanostructured (TNS) hybrids for oxygen and hydrogen evolution reactions. *Nano Res.* **2015**, *8*, 3725–3736. [[CrossRef](#)]
53. Vincent, I.; Kruger, A.; Bessarabov, D. Development of efficient membrane electrode assembly for low cost hydrogen production by anion exchange membrane electrolysis. *Int. J. Hydrogen Energy* **2017**, *42*, 10752–10761. [[CrossRef](#)]
54. Alsabet, M.; Grden, M.; Jerkiewicz, G. Electrochemical growth of surface oxides on nickel. Part 1: Formation of α-Ni(OH)₂ in relation to the polarization potential, polarization time, and temperature. *Electrocatalysis* **2011**, *2*, 317–330. [[CrossRef](#)]
55. Harrington, D. Complex Nonlinear Least Squares Fitting of Immittance Data. Available online: <https://www.maplesoft.com/applications/view.aspx?SID=154540> (accessed on 26 August 2019).



© 2019 by the authors. Licensee MDPI, Basel, Switzerland. This article is an open access article distributed under the terms and conditions of the Creative Commons Attribution (CC BY) license (<http://creativecommons.org/licenses/by/4.0/>).